

On the linear breakdown of Görtler vortices

A. BOTTARO and B. G. B. KLINGMANN*

ABSTRACT. – The linear stability of streamwise vortices in a boundary layer is studied with respect to perturbations of travelling wave form. The vortices considered here are those arising from a centrifugal instability (Görtler vortices), but the mechanisms involved in their breakdown are of general nature. Travelling wave instabilities are the first step towards transition to turbulence in boundary layers over concave walls, and may also provide insight into the mechanism by which turbulence is created and sustained in other wall-bounded flows.

The Görtler flow is calculated by solving the steady nonlinear boundary layer equations on a curved wall. The growth of Görtler vortices is initially governed by a linear centrifugal instability, up to a point where a strongly nonlinear reorganization of the flow field occurs, and typical “mushroom” structures develop. At this point, the spanwise-averaged velocity profile becomes inflexional and, at the same time, the spanwise shear increases rapidly near the “mushroom stems”. By applying a Floquet-type analysis locally at successive downstream stations, it is found that the secondary instability is of sinuous type at the onset, independently of the spanwise wave number, and that the onset coincides with the development of “mushroom” structures, or more precisely with the appearance of an inflexion point in the spanwise-averaged velocity distribution. Further downstream, several modes become unstable, and the most unstable frequency increases — a fact which is related to the increase in spanwise shear. When the spanwise wave number is large enough, the varicose mode of instability rapidly acquires importance, in correspondence with the intensification of vertical shear close to the “mushroom” hat, and it may eventually rule the instability development.

The theory is applied to a case simulating the experiments of Swearingen and Blackwelder (1987) *J. Fluid Mech.* **182**, 255, for which it correctly predicts the distribution of the perturbation velocity and the dominant frequency. In this case sinuous modes of instability predominate over varicose modes at all streamwise stations examined, but far enough downstream the varicose mode is found to affect a larger range of frequencies. The instabilities propagate at a speed which is typically 0.6-0.7 times the outer flow velocity, and their growth rates are quite large: amplitudes may grow by a factor of 3 within one wave length.

Varying the Reynolds number Re has only a minor influence on the sinuous mode, which implies that the secondary instability mechanism is mainly inviscid. Some influence appears on the varicose mode when the spanwise wave length is small: For progressively larger values of Re shorter waves become more unstable.

Finally, it is found that the effect of neglecting the cross-stream components of the base flow from the analysis does not modify the results in any substantial way, a fact which indicates that non-parallel effects can be neglected.

1. Introduction

A boundary layer developing along a concave surface is susceptible to a number of instabilities as the flow proceeds downstream. The first such instability is produced by an imbalance between centrifugal forces and restoring normal pressure gradients, and

* IMHEF-DGM, École Polytechnique Fédérale de Lausanne, CH 1015 Lausanne, Switzerland. Present address: Volvo Aerospace Corp., Space Division S-461 81 Trollhättan, Sweden.

leads to the formation of Görtler vortices. Vortices grow downstream and produce highly distorted velocity profiles such that a time-dependent secondary shear instability may be generated. Following this, higher instabilities, eventually leading to transition, appear. By understanding the physical features ruling the secondary instability of the Görtler problem, we also hope to isolate some possible basic mechanisms by which longitudinal vortices in shear flows (jets, wakes, boundary layers) break down.

A lot attention has been paid recently to secondary instability phenomena of Görtler vortices. One type of secondary instability, which we cite only in passing, has been examined recently by Guo and Finlay (1994) and considers spatially developing vortices subject to spanwise-periodic perturbations. This Eckhaus-type instability is responsible for interaction (merging and splitting) of vortex pairs and typically produces slanted vortices (see also Bottaro *et al.*, 1996). If vortices are steadily triggered near the leading edge of the plate in a low disturbance environment, the secondary instability that develops is normally a travelling wave packet. This kind of instability is the topic of the present paper. The most comprehensive experimental study of the subject was conducted by Swearingen and Blackwelder (1987), from now on referred to as SB, and several subsequent theories and computations have tried to reproduce the data presented by them. SB showed evidence for both sinuous and varicose type of secondary instability waves, and were able to relate the instability to inflectional mean flow velocity profiles. The sinuous mode was first analysed theoretically by Hall and Seddougui (1989) in the small spanwise wave-length asymptotic regime. Their results were later corrected and extended by Bassom and Seddougui (1990). Because of the asymptotic nature of these analyses, the results are mainly of academic interest: high wave number Görtler vortices are susceptible to a travelling wave secondary instability confined to a thin layer near the outer edge of the vortex. Even if, as pointed out by Hall and Seddougui, with the increase of the Görtler number "the small wave length regime is always approached by a fixed wave-length vortex pair in a growing boundary layer", available experimental evidence indicates that breakdown is typically observed for parameter values far from the asymptotic limits. Park (1990) and Park and Huerre (1995) studied the primary and secondary instabilities of a Görtler flow developing from a boundary layer with asymptotic suction at the wall. The steady vortical flow was computed from temporal simulations of the nonlinear boundary layer equations, and the secondary instability analysis of two-dimensional base profiles ($U(y, z; T)$, $V(y, z; T)$, $W(y, z; T)$) was performed at different fixed "downstream" times T . In their analysis, the cross-stream velocity components V and W were retained. For the spanwise wave-length examined, it was found that the sinuous mode was excited first, that a broad band of wave numbers was amplified, and that the streamwise velocity eigenfunctions were well correlated with the spanwise shear U_z . The varicose mode was amplified only at "downstream" times and was correlated with U_y . Hall and Horseman (1991) conducted a similar analysis in the inviscid limit, without inclusion of the cross-stream components V and W of the base flow or of all x -derivatives; this locally parallel approximation is asymptotically consistent. Also Hall and Horseman found the sinuous mode to be preferentially excited over the varicose mode of instability; a good qualitative agreement with the measurements of SB was reported. This should be taken as an indication that the

primary motor of the secondary instability is inviscid. Yu and Liu (1991, 1994) carried out an analysis in order to reproduce SB's results and included the viscous terms in the equations, which read in dimensionless form:

$$(1.1) \quad \nabla \cdot \mathbf{u} = 0,$$

$$(1.2) \quad \mathbf{u}_t + U\mathbf{u}_x + (vU_y + wU_z)\mathbf{e}_x = -\nabla p + \text{Re}^{-1}\nabla^2\mathbf{u}.$$

In the above $\mathbf{u} = (u, v, w)$ and p denote the infinitesimal perturbation field superimposed on the basic Görtler vortex flow $\mathbf{U} = (U, V, W)$, which was computed by Sabry and Liu (1991). The Reynolds number Re is defined with the free stream velocity U_∞ and a characteristic boundary layer length scale δ . In contrast to the problem governing the primary instability of Görtler vortices, here all velocities are scaled with the same reference speed U_∞ , and all lengths with the same reference length δ . Pressure is made nondimensional with ρU_∞^2 , ρ being the constant density. Also in Yu and Liu's analysis the sinuous mode was identified as being the most unstable, for a streamwise wave number fixed and equal to that reported by SB; the eigenfunctions of the streamwise velocity of Yu and Liu are quite similar to the measured u_{rms} . Sabry *et al.* (1990) proposed that the secondary instability of vortex flows can be approached in terms of the local stability of the shear profiles at a fixed y (the y chosen is typically the one of maximum normal vorticity). The results they presented were encouraging and led Le Cunff and Bottaro (1993) to consider the same kind of simplified analysis to explain the secondary instability of the Dean flow (Dean, 1928). The hypothesis brought forward, that the local analysis of simple shear profiles at one fixed y might be sufficient to interpret observed features of wavy vortices, is consistent with the fact that sinuous waves are related to $\frac{\partial U}{\partial z}$ (SB, Park 1990, Liu and Domaradzki 1993, Saric 1994) and it lends support to the idea that $\left(\frac{\partial U}{\partial z}\right)_{\max}$ is the proper scale for the frequency of the secondary instability. We will come back to this point later on.

Few works on the nonlinear development of the secondary instability are present in the literature. A weakly nonlinear analysis was performed by Seddougui and Bassom (1991) which showed that there exist stable flow configurations that support travelling waves of finite amplitude. The fully nonlinear temporal calculations of transition to turbulence by Liu and Domaradzki (1993) demonstrated that the main energy production mechanisms during the transition process are instabilities of wake-like spanwise shear layers centred around the upwash region of the vortices. Sinuous waves were observed first, and a varicose mode, in the form of hairpin vortices appeared at later "downstream" times.

Results from work carried out to date are fairly consistent and provide a first picture of the secondary instability of Görtler vortices. Some questions are still outstanding, however, and are addressed in the present paper; our aims are to

- (i) carry out local analyses of the secondary instability for a range of spanwise and streamwise wave-lengths, and for several streamwise locations;
- (ii) assess the influence of Re on the stability of the primary vortex state;

(iii) find out whether the inclusion of the cross-flow velocity components of the basic vortical flow has a noticeable influence on the results; in other words verify whether non-parallel effects are significant or not;

(iv) find a proper scaling for the frequency and wave-length of the secondary instability.

The paper is organized as follows. The problem is formulated in section 2; in section 3 we discuss the development and structure of the primary instability, followed by an analysis of the results for secondary instability modes at different spanwise wave numbers. Section 4 is devoted particularly to highlighting the importance of spanwise shear on the development of the sinuous instability mode, and some correlations for the predicted frequencies and wave numbers are introduced. Section 5 contains the conclusions.

2. Mathematical formulation

The development of steady vortices was first computed by solving the three-dimensional boundary layer equations with a nonlinear finite volume code. Linear stability was then performed on the flow field obtained at a given x -station, by expanding it in a Fourier series in the spanwise direction, and assuming the variations in the streamwise direction to be slower than the growth of the secondary instability. This approach is similar to that of Hall and Horseman (1991) and Yu and Liu (1991, 1994).

2.1. NONLINEAR DEVELOPMENT OF STEADY VORTICES

We consider the boundary layer flow over the concave wall (see Figure 1) with constant radius of curvature R and free stream velocity U_∞ . We introduce the length scale δ in

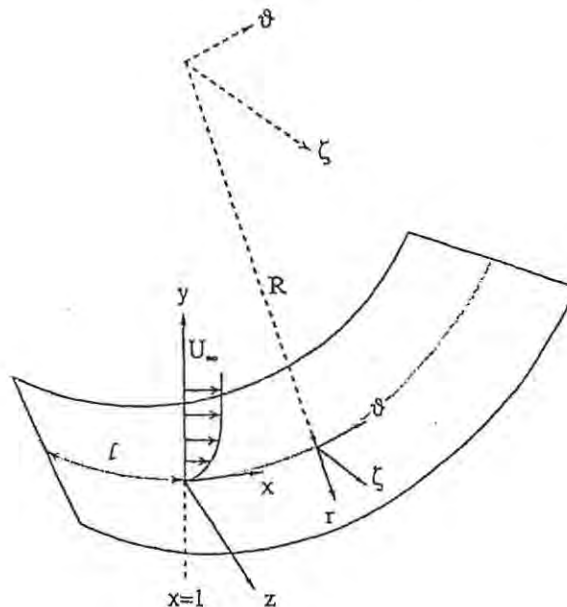


Fig. 1. – Sketch of the curved boundary layer.

the direction normal to the plate, defined as

$$\delta = \sqrt{\frac{\nu x}{U_\infty}},$$

where x is the streamwise distance from the boundary layer origin to a given downstream point, and ν the kinematic viscosity. The Reynolds number Re and the Görtler number G are defined by:

$$(2.1) \quad Re = \frac{U_\infty \delta}{\nu} \quad \text{and} \quad G = Re \sqrt{\frac{\delta}{R}}.$$

In a cylindrical coordinate system (r, θ, ζ) with corresponding velocity components (v_r, v_θ, v_ζ) , we introduce the dimensionless boundary layer coordinates X, y , and z :

$$(2.2) \quad X = \frac{R\theta}{x} = \frac{1}{Re} \frac{R\theta}{\delta}, \quad y = -\frac{(r-R)}{\delta}, \quad z = \frac{\zeta}{\delta},$$

and the dimensionless velocities $\mathbf{U} = (U, V, W)$ together with the pressure P :

$$(2.3) \quad U = \frac{v_\theta}{U_\infty}, \quad V = -\frac{v_r}{U_\infty} Re, \quad W = \frac{v_\zeta}{U_\infty} Re, \quad P = \frac{P'}{\rho U_\infty^2} Re^2$$

where ρ is the constant density and P' is the dimensional pressure. If we now assume that $x/R \rightarrow 0$ and $Re \rightarrow \infty$ in such a way that $G = O(1)$, the Navier-Stokes equations reduce at leading order in Re^{-1} to a parabolic system in which Re drops out:

$$(2.4) \quad \frac{\partial U}{\partial X} + \frac{\partial V}{\partial y} + \frac{\partial W}{\partial z} = 0,$$

$$(2.5) \quad \left[U \frac{\partial}{\partial X} + V \frac{\partial}{\partial y} + W \frac{\partial}{\partial z} \right] U = \frac{\partial^2 U}{\partial y^2} + \frac{\partial^2 U}{\partial z^2},$$

$$(2.6) \quad \left[U \frac{\partial}{\partial X} + V \frac{\partial}{\partial y} + W \frac{\partial}{\partial z} \right] V + G^2 U^2 = -\frac{\partial P}{\partial y} + \frac{\partial^2 V}{\partial y^2} + \frac{\partial^2 V}{\partial z^2},$$

$$(2.7) \quad \left[U \frac{\partial}{\partial X} + V \frac{\partial}{\partial y} + W \frac{\partial}{\partial z} \right] W = -\frac{\partial P}{\partial z} + \frac{\partial^2 W}{\partial y^2} + \frac{\partial^2 W}{\partial z^2},$$

with the boundary conditions:

$$(2.8a) \quad U = V = W = 0 \quad \text{at} \quad y = 0,$$

$$(2.8b) \quad U_y = V_y = W_y = 0 \quad \text{as} \quad y \rightarrow \infty.$$

This system is solved numerically using the finite volume procedure described in Patankar and Spalding (1972). For this purpose, the y and z coordinates are normalized at the

fixed downstream position x_0 , at which $X = 1$ and $\delta = \delta_0$. The computational y -domain is truncated at $y_e = 50$. Because of spanwise symmetry the computations need to be performed only over half a wave-length, and appropriate boundary conditions are:

$$(2.8c) \quad U_z = V_z = W = 0 \quad \text{for } z = 0, \lambda_z/2.$$

Another measure of the wave-length is Λ , defined as:

$$\Lambda = \frac{U_\infty R}{\nu} \left(\frac{\lambda_z}{R} \right)^{3/2} = G \left(\frac{2\pi}{\beta} \right)^{3/2},$$

with $\beta = 2\pi\delta/\lambda_z$ the spanwise wave number. The quantity Λ is dimensionless and remains constant with G (and X).

The computational $y - z$ domain is divided into rectangular cells with the grid points located at the geometric centres of the cells. The discretized equations are obtained by integrating the conservation equations over control volumes having these cells as a base and extending a distance ΔX in the streamwise direction. The velocity components V and W are defined at staggered locations, so as to avoid unrealistic pressure fields and associated numerical instabilities. Local linear y and z dependence in any of the primitive variables is assumed, resulting in a second order accurate scheme. For the parameter values of this work, we have determined that a 71×25 $y - z$ grid (stretched in y and uniform in z) is adequate (see Bottaro *et al.*, 1996).

Since the equations are parabolic, the solution can be obtained by streamwise marching, which is accomplished through a fully implicit first order forward Euler scheme. In the present work we have used a step $\Delta X = 0.02$. The upstream boundary conditions are obtained by solving the local linear stability equations for $G = G_0$, and then imposing the solution at $X = 1$. The initial spatial development is in excellent agreement with results obtained by downstream marching of the linear parabolic equations (*cf.* Bottaro *et al.*, 1996). Since "mushroom"-shaped flow structures develop, we will, henceforth, use the somewhat loose definitions of mushroom's stem and hat. At the mushroom's stem the secondary flow moves away from the wall; the alternative definition of outflow or upwash is also employed. At the hat (or turn-over region) the projection of the streamlines on a cross-sectional plane, for some z -range centered on the stem's position and at a value of y equal to approximately the boundary layer thickness, show trajectories that start bending back to close the vortex loop.

2.2. STABILITY ANALYSIS

The steady Görtler flow is now analyzed with respect to time-dependent secondary instabilities. At each given X -station, the steady $y - z$ flow field $\mathbf{U} = \mathbf{U}(y, z; X)$ is assumed to be susceptible to travelling waves of the form

$$(2.9) \quad \mathbf{u}(x, y, z, t) = \hat{\mathbf{u}}(y, z) e^{i(\alpha x - \omega t)},$$

where ω is the frequency of the wave, α is the streamwise wave number, and x is defined as

$$x = \frac{R\theta}{\delta}.$$

The streamwise and spanwise wave lengths are both scaled with δ . The perturbation velocities $\mathbf{u} = (u, v, w)$ are thought to be small enough to be linearly superimposed onto the steady Görtler flow, and they are taken to be of the same order of magnitude. This implies that the Reynolds number must be reintroduced, while the curvature must be neglected.

Here, we have chosen to formulate the problem using the equations for the vorticity components in order to eliminate the pressure. According to the scaling relations (2.2, 2.3), the streamwise variation of \mathbf{U} is assumed to be much smaller than variations in the $y - z$ plane (an *a posteriori* check on the obtained flow fields shows that this assumption is well justified). Neglecting the streamwise derivatives of V and W , the vorticity associated with \mathbf{U} is

$$\Xi = \begin{pmatrix} \frac{1}{\text{Re}} \left(\frac{\partial W}{\partial y} - \frac{\partial V}{\partial z} \right) \\ \frac{\partial U}{\partial z} \\ \frac{\partial U}{\partial y} \end{pmatrix} + O(\text{Re}^{-2}),$$

and if we denote the vorticity associated with \mathbf{u} by $\xi = (\xi, \eta, \kappa)$, the linearized disturbance equations for the normal and spanwise vorticity are, to the same order of accuracy:

$$(2.10) \quad \begin{aligned} & \left[\frac{\partial}{\partial t} + U \frac{\partial}{\partial x} + \frac{V}{\text{Re}} \frac{\partial}{\partial y} + \frac{W}{\text{Re}} \frac{\partial}{\partial z} \right] \eta + \left[u \frac{\partial}{\partial x} + v \frac{\partial}{\partial y} + w \frac{\partial}{\partial z} \right] \frac{\partial U}{\partial z} \\ & - \left[\frac{1}{\text{Re}} \left(\frac{\partial W}{\partial y} - \frac{\partial V}{\partial z} \right) \frac{\partial}{\partial x} + \frac{\partial U}{\partial z} \frac{\partial}{\partial y} - \frac{\partial U}{\partial y} \frac{\partial}{\partial z} \right] v \\ & - \left[\eta \frac{\partial}{\partial y} + \kappa \frac{\partial}{\partial z} \right] \frac{V}{\text{Re}} = \frac{1}{\text{Re}} \nabla^2 \eta + O(\text{Re}^{-2}), \end{aligned}$$

$$(2.11) \quad \begin{aligned} & \left[\frac{\partial}{\partial t} + U \frac{\partial}{\partial x} + \frac{V}{\text{Re}} \frac{\partial}{\partial y} + \frac{W}{\text{Re}} \frac{\partial}{\partial z} \right] \kappa - \left[u \frac{\partial}{\partial x} + v \frac{\partial}{\partial y} + w \frac{\partial}{\partial z} \right] \frac{\partial U}{\partial y} \\ & - \left[\frac{1}{\text{Re}} \left(\frac{\partial W}{\partial y} - \frac{\partial V}{\partial z} \right) \frac{\partial}{\partial x} + \frac{\partial U}{\partial z} \frac{\partial}{\partial y} - \frac{\partial U}{\partial y} \frac{\partial}{\partial z} \right] w \\ & - \left[\eta \frac{\partial}{\partial y} + \kappa \frac{\partial}{\partial z} \right] \frac{W}{\text{Re}} = \frac{1}{\text{Re}} \nabla^2 \kappa + O(\text{Re}^{-2}), \end{aligned}$$

where ∇^2 denotes $\left(\frac{\partial^2}{\partial x^2} + \frac{\partial^2}{\partial y^2} + \frac{\partial^2}{\partial z^2} \right)$, $\eta = \left(\frac{\partial v}{\partial z} - \frac{\partial w}{\partial x} \right)$ and $\kappa = \left(\frac{\partial v}{\partial x} - \frac{\partial u}{\partial y} \right)$.

In the course of the present work, it will be shown that the secondary instability is insensitive to the Reynolds number, a fact which also justifies the neglect of V and W terms. Most calculations were therefore carried out setting $V = W = \partial U / \partial x = 0$.

In the spanwise direction, U and u are expanded into Fourier series in harmonics of the spanwise wave number β :

$$(2.12) \quad U(y, z; X) = \bar{U}_0(y; X) + \sum_{n=1}^N \bar{U}_n(y; X)(e^{+in\beta z} + e^{-in\beta z}),$$

$$(2.13) \quad \hat{u}(y, z) = \bar{u}_0(y) + \sum_{n=1}^N \{\bar{u}_{+n}(y)e^{+in\beta z} + \bar{u}_{-n}(y)e^{-in\beta z}\}.$$

Up to five harmonics ($N \leq 5$) were used in the present work. Because of the symmetry of the base flow about the stem, either sinuous or varicose modes can appear and the coefficients of the function \hat{u} —from now on simply termed $\mathbf{u} = (u, v, w)$ —are related by

$$\begin{aligned} \bar{u}_{+n} &= \bar{u}_{-n}, & \bar{\mathbf{u}}_0(y) &= (\tilde{u}_0, \tilde{v}_0, 0) & \text{(varicose mode)} \\ \bar{u}_{+n} &= -\bar{u}_{-n}, & \bar{\mathbf{u}}_0(y) &= (0, 0, \tilde{w}_0) & \text{(sinuous mode).} \end{aligned}$$

At the inception of a sinuous mode, out-of-phase fluctuations of the streamwise velocity on either side of the upwash region near the wall induce oscillations in w , which produce meandering of the low speed streak in a horizontal plane (see flow visualizations by Bippes, 1978). In the varicose mode the fluctuations of u near the mushroom hat become important, and induce in-phase oscillations of v and w on the two sides of the upwash plane; varicose fluctuations seem to be related to the downstream observation of horseshoe shaped vortices (Aihara, 1993; Liu and Domaradzski, 1993).

The base flow and the disturbances (2.9) as expanded by (2.12) and (2.13), are inserted into the linearized equations (2.10) and (2.11). A further simplification consists of eliminating \bar{w}_n from the unknowns by using the continuity equation (1.1): Thus we end up with a system of equations in \bar{u}_n and \bar{v}_n in which terms pertaining to each multiple of β are grouped together with the help of *Mathematica* (Wolfram, 1991). This equation set defines the dispersion relation between α and ω . The amplification of the wave is accounted for by taking either ω complex and α real (temporal stability) or α complex and ω real (spatial stability). The temporal problem reduces to a linear eigenvalue problem for ω . The spatial stability characteristics can be obtained by iterating the temporal problem until the condition that ω be real is satisfied. Although some spatial calculations have been performed, they are much more CPU-intensive and we have thus chosen to conduct an extensive parametric study by using only the temporal stability approach.

The system of equations for $\bar{u}_n(y)$ and $\bar{v}_n(y)$ is formulated with a spectral Chebyshev collocation method after a suitable mapping transformation. The physical domain ($y : 0 \rightarrow \infty$) is transferred onto ($y_T : -1 \rightarrow 1$) by the transformation $y_T = 1 - 2e^{-y/y_0}$,

where y_0 is chosen such that the outmost y -point is at $y = 50$, and the Chebyshev polynomials are evaluated at the M collocation points

$$y_T = -\cos \frac{j\pi}{M+1}, \quad j = 0, \dots, M.$$

M is typically taken equal to 80. The resulting generalized eigenvalue problem is solved with the routine F02GJE, a QZ-algorithm from the NAG library, to yield the M modes (interested readers are referred to Klingmann 1993 for more details of the numerical procedure). Spurious roots are present but can easily be identified and eliminated since such unphysical solutions do not converge when M is increased.

3. Development and structure of the instability

Görtler vortices start developing when the Görtler number exceeds a certain threshold, which varies depending on the spanwise wave number. The instability is operational within a wide range of spanwise wave-lengths ranging from $\Lambda = 100$ to 1000. According to linear stability theory, vortices with $\Lambda = 200$ are most strongly amplified, however, most experimental observations have been made at larger wave-lengths. For the present study, we focus on the three cases $\Lambda = 160, 450$ and 1000. These values are representative of typical wave-lengths found in experiments, and allow an appreciation of the dominant secondary instability effects (sinuous or varicose symmetry) for a large range of spanwise scales of the primary instability.

The present computations for $\Lambda = 450$ reproduce accurately previous computations by Sabry and Liu (1991), Lee and Liu (1992), Liu and Domaradzki (1993) and experimental results in SB. All the calculations start 40 cm downstream of the leading edge of the curved plate (the dimensionless coordinate X is scaled with this position), and the inlet conditions imposed come from the solution of the local, nonparallel linear stability problem (Floryan & Saric 1984) for $\Lambda = 450$ and $G = 6.756$, with an initial amplitude of $U/U_{\text{Blas}} = 4.1\%$ where U_{Blas} denotes the velocity distribution in a Blasius boundary layer. This procedure may be justified by the excellent agreement between the linear and nonlinear solutions obtained by Bottaro *et al.* (1996) up to quite high G . The Reynolds number defined by equation (2.1) is equal to 365 at the initial X position. Re , G and β increase downstream as shown in Table I.

TABLE I. – Flow parameters at different downstream stations.

x (cm)	X	δ (cm)	G	Re	β ($\Lambda = 160$)	β ($\Lambda = 450$)	β ($\Lambda = 1000$)
40	1.0	0.109	6.756	365	0.762	0.382	0.225
72	1.8	0.147	10.50	490	1.023	0.513	0.301
80	2.0	0.155	11.33	515	1.078	0.541	0.318
88	2.2	0.162	12.21	542	1.126	0.565	0.332
96	2.4	0.170	13.01	565	1.188	0.593	0.348
104	2.6	0.177	13.86	590	1.236	0.617	0.362

The linear and nonlinear development of Görtler vortices at different spanwise wave-numbers has been discussed by Bottaro *et al.* (1996). The vortices first go through a phase of nearly exponential growth, followed by a nonlinear reorganization phase, during which the typical mushroom-like structures develop. During this phase, the energy begins to level off, finally leading to a state where the energy saturates at a constant level. It is during this phase that the flow becomes susceptible to secondary wave instabilities.

Figure 2 shows the evolution of the relative perturbation energy $E = e/e_0$ for these three wave lengths, with e defined by

$$(3.1) \quad e = \frac{1}{2} \int_0^{\lambda_z/2} \int_0^{y_e} (U - U_{\text{Blas}})^2 dy dz,$$

where e_0 represents the initial energy at X_0 .

The two cases $\Lambda = 160$ and 450 are quite similar. Initially, the energy grows at about the same rate, and it begins to level off at about $X = 2$. However, the saturation level of E is larger for $\Lambda = 450$ than for $\Lambda = 160$. The curve for $\Lambda = 1000$ reaches about the same saturation levels as $\Lambda = 450$, but further downstream. The nonlinear development also leads to a decrease of the wall shear stress, $(\partial U/\partial y)_{\text{wall}}$, at the “stem” of the mushroom structure (outflow region, $z = \lambda_z/2$) and a corresponding increase in the region between two mushroom structures (inflow region, $z = 0$). This is shown in Figure 2-right. The wall shear stress at $z = 0$ levels off at approximately the same position as E , while in the outflow region it first decreases and then increases again. The minimum occurs before the energy saturation, and is at $X = 1.9, 2.0$ and 2.35 for the three wave lengths $\Lambda = 160, 450$ and 1000 , respectively.

In the remainder of the paper we will try to cast light on the conditions necessary to initiate a wave instability. We will investigate the stability of the flow field at successive downstream positions and relate the onset and characteristics of the instability with features of the basic flow field.

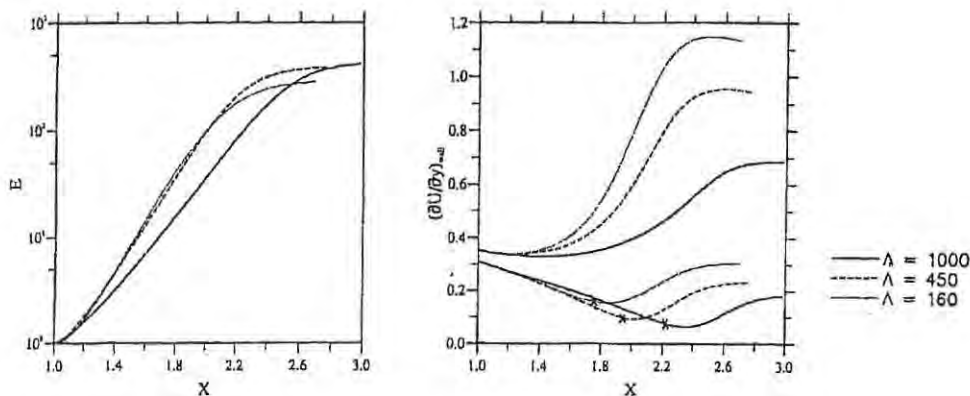


Fig. 2. – Downstream development of energy E and wall shear stress $(\partial U/\partial y)_{\text{wall}}$ at upwash ($z = \lambda_z/2$) and downwash ($z = 0$) positions for Görtler vortices with $\Lambda = 160, 450$ and 1000 .

3.1. DEVELOPMENT OF GÖRTLER VORTICES FOR $\Lambda = 160$

For Görtler vortices with $\Lambda = 160$, the formation of mushroom structures takes place between $X = 1.8$, where the energy first begins to depart from the quasi-exponential growth, and 2.4 where it saturates. The corresponding Görtler numbers are $G = 10.5$ and 13. The development of the flow field in this region is shown in Figure 3. In this, and all the following figures of the same type showing isolines, the variable on the horizontal scale is $2z/\lambda_z$ ($\in [0, 1]$ for half a vortex pair) and $\eta = y/\delta$ for the vertical scale (η is the Blasius similarity variable). The mushroom formation is most clearly seen in the isolines of U (Fig. 3a). There is an outflow region at $z = \lambda_z/2$, where fluid is being pumped out of the boundary layer, and an inflow region at $z = 0$, where the boundary layer becomes thinner with the increase of X . Figure 3b shows how this results in a concentration of spanwise shear $\partial U/\partial z$ near the outflow region ($z = \lambda_z/2$). Downstream of $X = 2.0$,

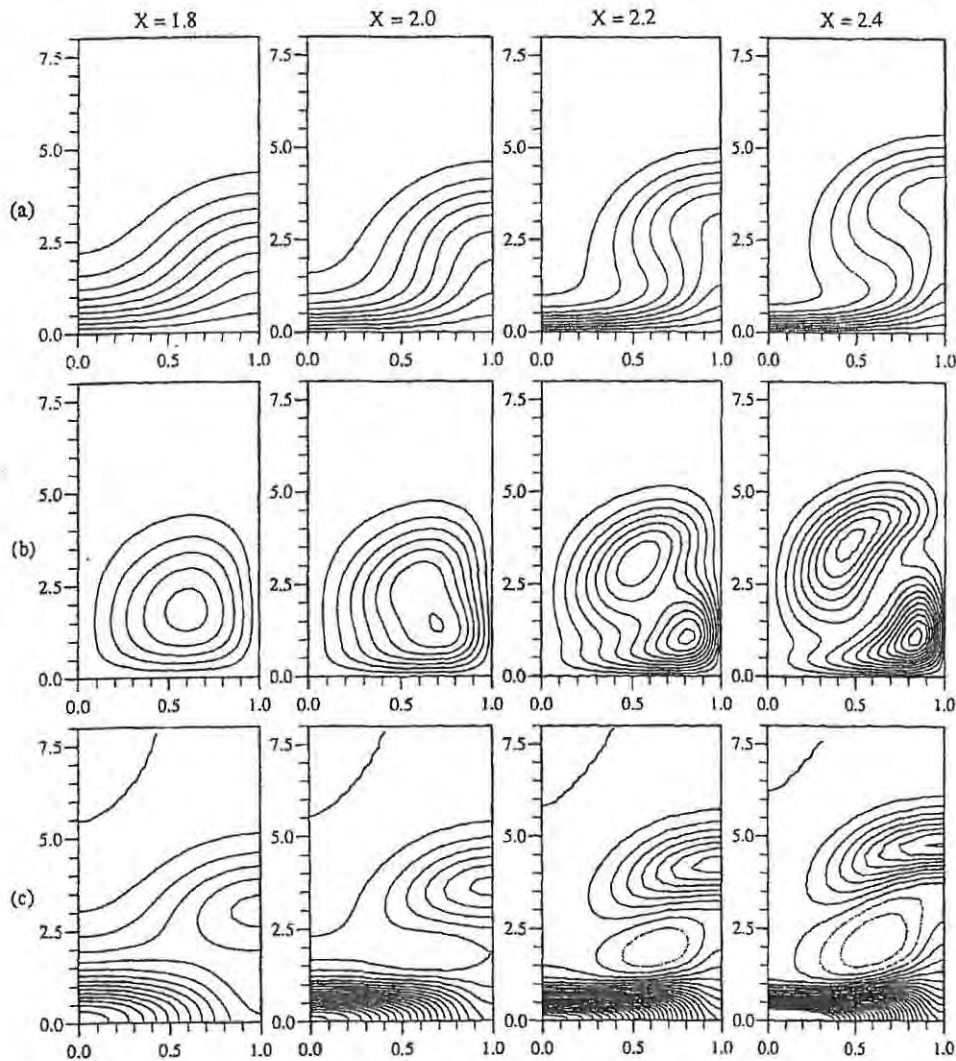


Fig. 3. - $\Lambda = 160$: Downstream development of Görtler vortices. Isolines in the (η, z) -plane of U (a), $|\partial U/\partial z|$ (b) and $\partial U/\partial y$ (c). Isolines of U are spaced 0.1 apart; isolines of spanwise and normal rate of shear strain are spaced 0.05 apart. Negative values are shown with dotted lines. Figures are not to scale.

two separate regions of $\partial U/\partial z$ can be clearly distinguished, one near the outflow region, and one near the mushroom "hat" ($z = \lambda_z/4$). We call this latter region the "turn-over" region, since the secondary flow turns at this point and is directed towards the wall. This can also be seen in the isolines of $\partial U/\partial y$ (Fig. 3c), where negative values appear at $X > 2.0$. Simultaneously, the wall-normal distribution of U becomes inflexional, first in the outflow region and further downstream in a broad region below the turn-over region (or mushroom 'hat'). In the outflow region, U is inflexional already at $x = 1.8$, but the spanwise mean profile, $\tilde{U}_0(y; X)$, does not become inflexional until $X = 2.0$. This is shown in Figures 4a and 4b, which display the profiles of $\tilde{U}_0(y; X)$ and $\partial^2 \tilde{U}_0/\partial y^2$ at $X = 1.8$ and 2.0, and the isolines of $\partial^2 U/\partial y^2$.

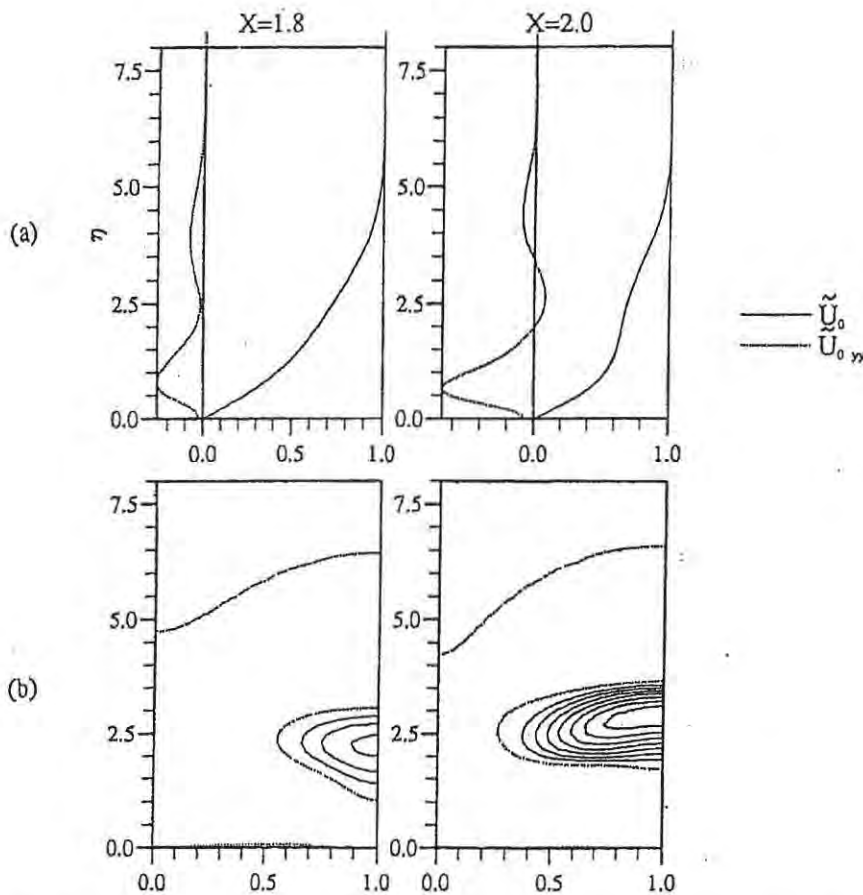


Fig. 4. - $\Lambda = 160$: Development of an inflexion in the y -distribution of U . (a) Profiles of $\tilde{U}_0(\eta; X)$ and $\partial^2 \tilde{U}_0/\partial y^2$. (b) Isolines of $\partial^2 U/\partial y^2$ in the (η, z) -plane. Only the positive values are shown with increment 0.025, while the zero levels are plotted with dotted lines.

The development of the local velocity profiles U at $z = 0$ and $\lambda_z/2$ is shown in Figure 5, where we also have included $\tilde{U}_0(y; X)$ and the 2D Blasius boundary layer profile. The velocity deficit in the outflow region is first centred near the middle of the boundary layer ($\eta \approx 2.5$), but begins to move out of the boundary layer at $X > 2.2$. The profiles for the successive spanwise harmonics $n = 1, \dots, 5$ are shown in Figure 5b.

The maximum in the first harmonic ($n = 1$, which can be interpreted as the *rms*-distribution along the span) first moves away from the wall, and eventually splits into a near wall part and a part associated with the velocity deficit at the mushroom "hat". A similar development can be seen for the higher harmonics. If the spanwise decomposition of the flow is interpreted in terms of a basic flow $\tilde{U}_0(y; X)$ and a perturbation flow $U' = \tilde{U}_n(y; X)$, $n > 0$, the development in Figure 5b can be seen as a concentration of Reynolds stress $U'V'\partial\tilde{U}_0/\partial y$ near the wall and near the boundary layer edge, which may be expected also in the structure of the secondary instability.

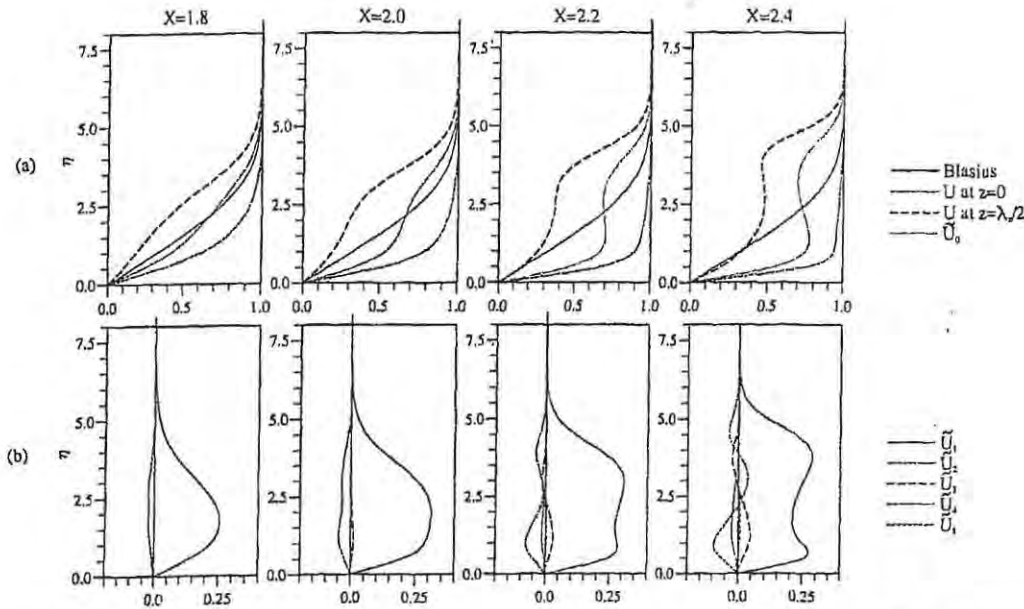


Fig. 5. - $\Lambda = 160$: Spanwise structure of the Görtler vortices at four X positions. (a) $\tilde{U}_0(\eta; X)$ and $U(\eta; z)$ at $z = 0$ and $\lambda_z/2$, 2D Blasius boundary layer profile. (b) spanwise harmonics of $U(\eta)$.

3.2. SECONDARY STABILITY CHARACTERISTICS FOR $\Lambda = 160$

The number of spanwise harmonics to be included in the secondary stability analysis can be estimated from Figure 5b, e.g. at $X = 1.8$, $N = 2$ should be sufficient to represent the flow field, whereas at $X = 2.4$, convergence can only be expected for $N \geq 5$. Figure 6 shows the convergence of the temporal eigenvalues for the sinuous mode at $X = 2.0$ and 2.2 as N is increased from 1 to 5. The streamwise wave number α is chosen close to the one which gives the most amplifying solution. At both stations, reasonable convergence is obtained with $N \geq 3$. In the following, $N = 5$ will be used throughout.

Figure 7 compares the temporal growth rates of the secondary stability for $\Lambda = 160$ as a function of frequency at three different downstream positions. We have plotted the eigenvalues as growth rates (ω_i) versus frequency (ω_r), obtained by varying the streamwise wave number α . This representation was motivated by the desire to compare immediately the ω_r of maximum amplification at each X with the most readily available experimental data; the frequency of the secondary instability. Furthermore, the results indicate that the nature of the secondary instability waves at each X is not very

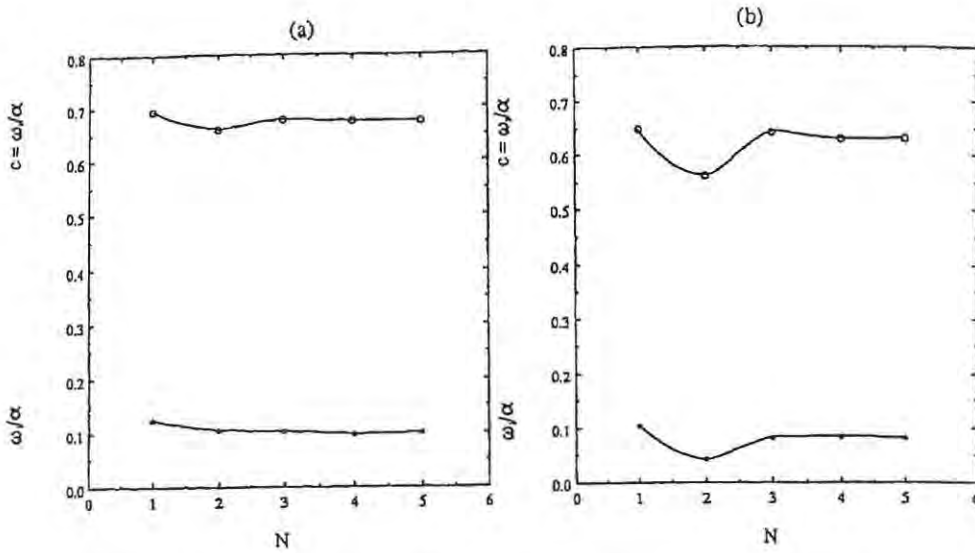


Fig. 6. - $\Lambda = 160$: Convergence of the temporal eigenvalues for the sinuous mode. (a) $X = 2.0, \alpha = 0.5$. (b) $X = 2.2, \alpha = 0.65$.

dispersive in the range of α considered so that plots of ω_r with α would provide little useful information (*cf.* also results obtained by Hall and Horseman, 1991; Le Cunff and Bottaro, 1993); instead we have chosen to indicate on Figure 7 (and subsequent figures of the same type) the value of the almost constant phase velocity $c = \omega_r/\alpha$ for each mode plotted at a given X . The onset of the instability is just downstream of $X = 1.8$, which coincides with the X -station where $\tilde{U}_0(y; X)$ develops an inflexion point. It is also close to the point where the wall shear stress at $z = \lambda_z/2$ reaches its minimum. It is the sinuous mode which first becomes unstable, whereas the varicose mode is stable up to $X = 2.2$, and its growth rate is much smaller than that of the sinuous mode. The range of unstable frequencies increases downstream, and so does the value of the most unstable frequency, which goes from $\omega_r = 0.10$ at $X = 1.8$ to $\omega_r = 0.41$ for $X = 2.2$. There is also a slight increase in the phase velocity from 0.62 to 0.68 with downstream distance.

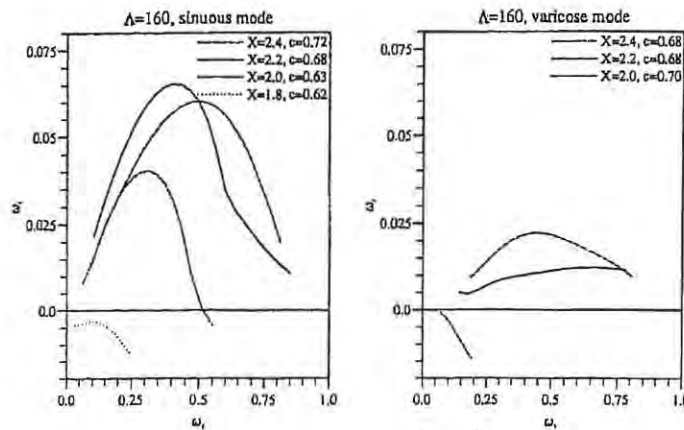


Fig. 7. - $\Lambda = 160$: Downstream development of the temporal growth rates for the secondary instability.

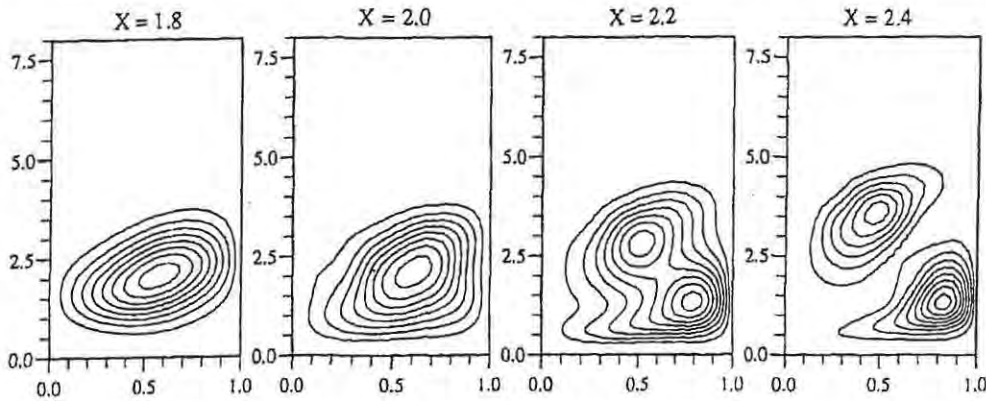


Fig. 8. - $\Lambda = 160$: Isolines of $|u|$ for the most unstable sinuous solutions at four values of X (10 isolines are plotted, equally spaced between maximum and minimum values).

Figure 8 shows the amplitude of u , a quantity which can be correlated with the experimentally measured u_{rms} , for the most unstable eigenmode at each X . Note that this figure does not describe the **spatial** development of the secondary instability since the frequency varies from frame to frame (the same applies to figures displaying similar results at other values of Λ to be shown later). We observe that the isolines in Figure 8 are well correlated with the development of the spanwise shear $\partial U/\partial z$ in Figure 3b, *i.e.* the maxima for both contour fields coincide approximately at all four X -positions. At $X = 2.2$, the maximum splits into two peaks at $(2z/\lambda_z, y/\delta) = (0.5, 3.0)$ and $(0.8, 1.3)$, which also coincides well with the peaks in $|\partial U/\partial z|$. The most unstable (or least stable) modes at each value of X are characterised by: at $X = 1.8$: $c = 0.62$, $\omega_r = 0.10$, $\omega_i = -0.003$ (the mode is damped); at $X = 2.0$: $c = 0.63$, $\omega_r = 0.30$, $\omega_i = 0.040$; at $X = 2.2$: $c = 0.68$, $\omega_r = 0.41$, $\omega_i = 0.065$; finally at $X = 2.4$ we have: $c = 0.72$, $\omega_r = 0.60$, $\omega_i = 0.060$.

As the complexity of the flow field increases, the number of unstable modes in the eigenvalue spectrum increases, and the spectra become more difficult to interpret. The results at $X = 2.4$ should, however, be interpreted with caution, since $N = 5$ is just

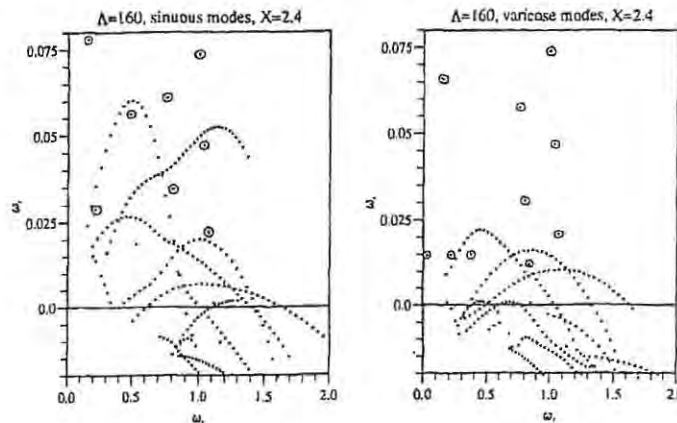


Fig. 9. - Temporal eigenvalue spectrum at $X = 2.4$. Unphysical spurious modes are circled for identification.

sufficient to represent the spanwise variations of the flow field correctly (cf. Figure 5b). Figure 9 shows a compilation of the eigenvalue spectra computed for α ranging from 0.05 to 2.25 at $X = 2.4$. The different modes form coherent groups which can also be identified on the basis of their phase velocity, $c = \omega_r/\alpha$. For example, the most amplified mode at $\omega_r = 0.5$ has $c = 0.72$, and is shown in Figure 8, whereas the dominating mode at $\omega_r = 1$ has $c = 0.59$, and a $|u|$ distribution which is completely confined to a near-wall region near the outflow, see Figure 10a. Isolines of $|u|$ for the two varicose modes are shown in Figure 10b and c. Both of them present maximum values in the outer part of the boundary layer near $z = 0.25\lambda_z$, i.e. in the turn-over region. At frequencies around 0.5, the most amplified varicose mode in Figure 10b is fairly well correlated with the $\partial U/\partial y$ field on Figure 3c, although this may be more of a visual impression due to the symmetry. For the high frequency mode (Fig. 10c), u is almost zero on the symmetry lines $2z/\lambda_z = 0$ and 1, but correlates remarkably well with the outer maximum of $\partial U/\partial z$ on Figure 3b.

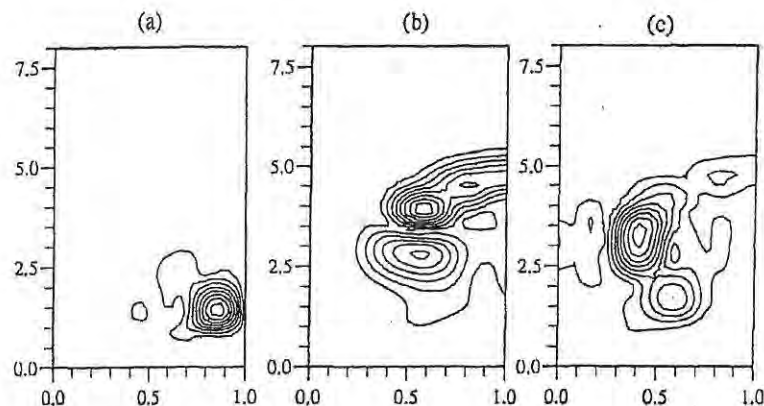


Fig. 10. - $\Lambda = 160$: Isolines of $|u|$ for higher modes at $X = 2.4$: (a) 2nd sinuous mode: $c = 0.59$, $\omega_r = 1.15$, $\omega_i = 0.052$; (b) 1st varicose mode: $c = 0.68$, $\omega_r = 0.45$, $\omega_i = 0.022$; (c) 2nd varicose mode: $c = 0.75$, $\omega_r = 0.85$, $\omega_i = 0.016$.

3.3. DEVELOPMENT AT $\Lambda = 450$

For $\Lambda = 450$, the downstream development of the vortices is similar to the case studied above, and also the secondary instability shows the same general trends. This case is of particular interest, since it allows a direct comparison with the experiments of SB. The secondary instability was observed between $x = 90$ and 100 cm, which corresponds to $2.25 < X < 2.5$ in the present calculation. Detailed measurements of the flow field were made at $x = 80, 90$ and 100 cm ($X = 2, 2.25, 2.5$). The dominant frequency found by SB at $x = 100$ cm was $F = 130$ Hz corresponding to $\omega_r = 0.283$, and the observed streamwise wave-length was about $\lambda_x = 2.5$ cm which gives $c = 0.650$ (*).

(*) The following relations apply: $\omega_r = \frac{2\pi\delta F}{U_\infty}$ and $\alpha = \frac{2\pi\delta}{\lambda_x}$, so that $c = \omega_r/\alpha$.

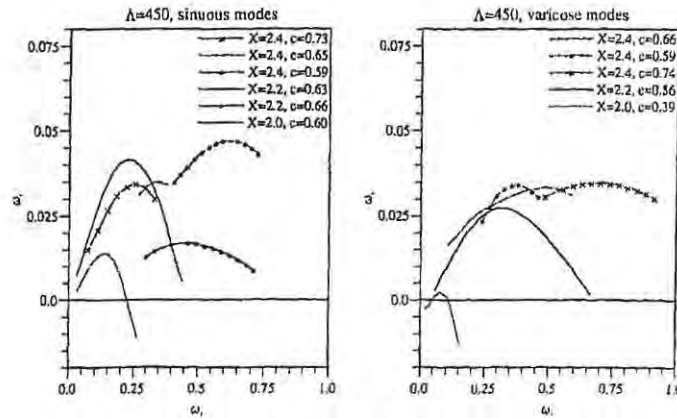


Fig. 11. - $\Lambda = 450$: Downstream development of the temporal growth rates for the secondary instability.

The temporal eigenvalues calculated at different X -stations are shown in Figure 11. The onset of the instability is between $X = 1.8$ and 2.0 ($x = 72$ and 80 cm), but, naturally, in an experiment, almost neutral disturbances can not be observed visually. The flow first becomes unstable with respect to the sinuous mode. The varicose mode begins to amplify at $X = 2.0$, and at $X = 2.4$ its growth rate becomes comparable to that of the sinuous mode. For both types, the frequency as well as the phase velocity

TABLE II. - Secondary stability characteristics for $\Lambda = 450$; α and λ_x represent the predictions of streamwise wave number (scaled with the local δ) and length for the maximum value of the temporal amplification ω_i in the present work, whereas Liu and Domaradzki fixed α at 0.534, and Yu and Liu fixed it at 0.408.

	X	x (cm)	δ (cm)	α	ω_r	ω_i	c	F (Hz)	λ_x (cm)
Sinuous waves									
SB (1987)		100	0.173	0.435	0.283	-	0.65	130	2.5
LD (1993)		96	0.170	0.534	0.413		0.80	200	2.0
YL (1991)		90	0.164	0.408	0.284	0.051	0.70	140	2.5
YL (1994, inviscid)		90	0.164	0.408	0.288	0.055	0.71	140	2.5
present results	2.2	88	0.162	0.365	0.23	0.042	0.63	110	2.8
	2.4	96	0.170	0.35	0.26	0.035	0.73	120	3.1
	2.4	96	0.170	0.53	0.35	0.035	0.66	160	2.0
	2.4	96	0.170	1.05	0.62	0.047	0.59	290	1.0
Varicose waves									
YL (1991)		90	0.164	0.408	0.277	0.032	0.68	135	2.5
YL (1994, inviscid)		90	0.164	0.408	0.284	0.028	0.70	135	2.5
present results	2.2	88	0.162	0.58	0.32	0.027	0.63	160	1.7
	2.4	96	0.170	0.60	0.35	0.034	0.59	165	1.8
	2.4	96	0.170	0.75	0.50	0.035	0.66	235	1.4
	2.4	96	0.170	0.92	0.68	0.035	0.74	320	1.2

of the most amplified waves increase with X . At $X = 2.2$, the most amplified mode is sinuous, with a frequency of $\omega_r = 0.22$ and $c = 0.63$, in excellent agreement with the experiment of SB. The eigenvalues obtained are also in good agreement with those previously calculated by Yu and Liu, where the flow field computed by Sabry and Liu was analyzed at an X -station corresponding to $x = 90$ cm. The eigenvalues obtained here and in comparable studies are reported in Table II for both symmetry cases. Notice that a scaling based on the local δ has been used throughout, whereas in their work Yu and Liu have scaled the results with $\delta_0 = \delta(x_0)$.

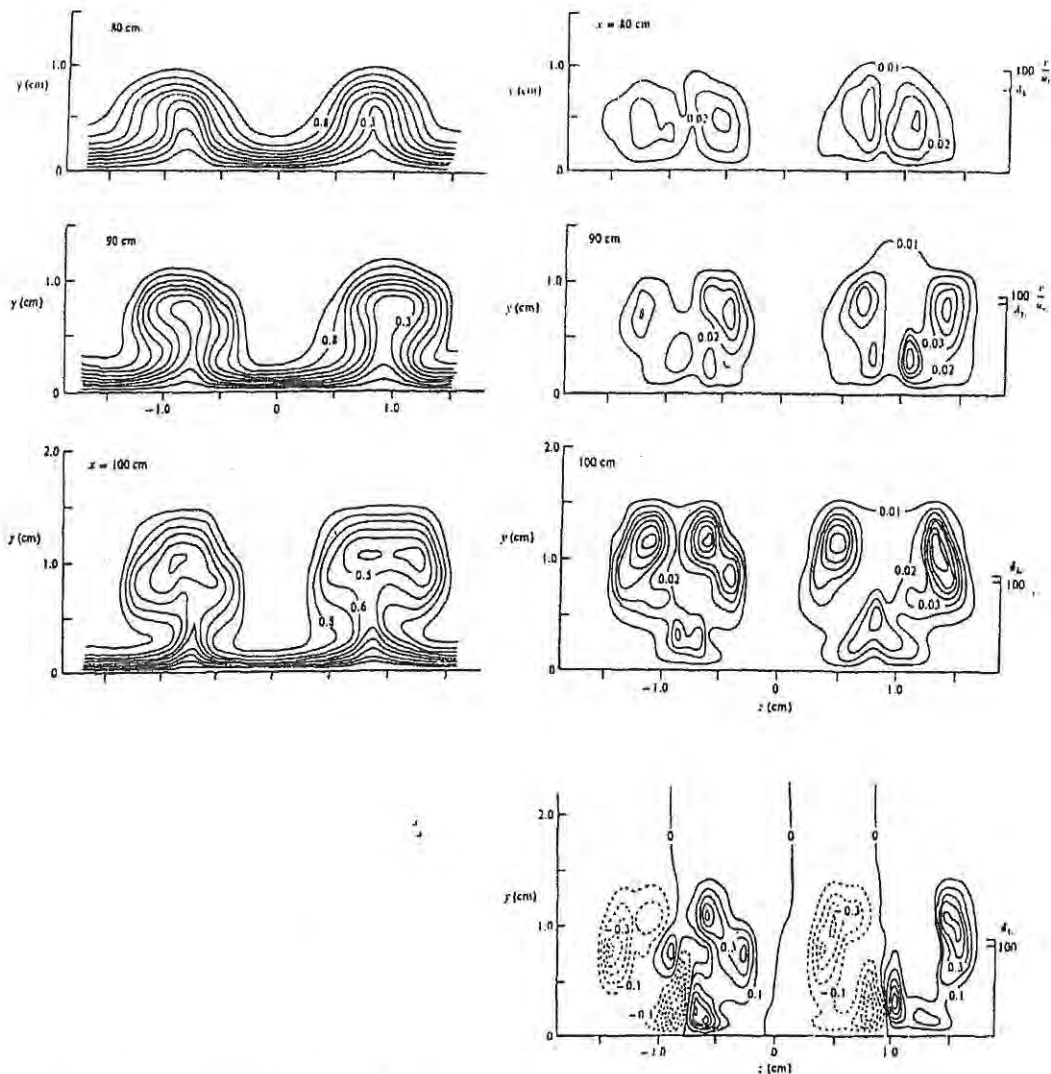


Fig. 12. – Isolines of U measured by SB at $x = 80, 90$ and 100 cm (left column) and u_{rms} at the same stations (right column). The figure on the bottom, right, is the spanwise rate of strain $\partial U / \partial z$ at $x = 100$ cm.

The mean and fluctuating flow fields measured by SB are shown in Figure 12, together with isolines of the spanwise shear at $x = 100$ cm, while Figure 13 shows the X -development according to the present calculations, and also gives the contours of $|u|$ for

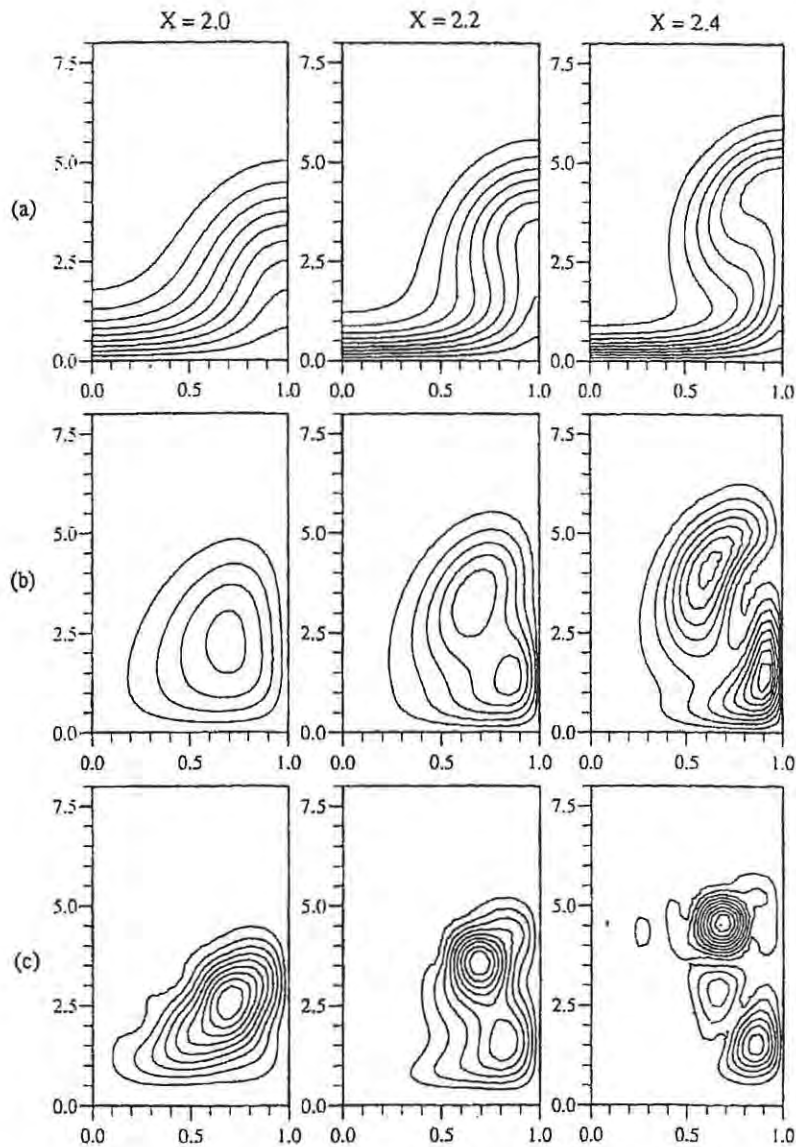


Fig. 13. - $\Lambda = 450$: Downstream development of U (a), $|\partial U / \partial z|$ (b) and $|u|$ (c) of the most unstable sinuous modes at three values of X . Figures not to scale.

the most amplified sinuous eigenmodes. The results for the unstable modes at the values of X considered are the following. At $X = 2.0$: $c = 0.60$, $\omega_r = 0.13$, $\omega_i = 0.014$; at $X = 2.2$: $c = 0.63$, $\omega_r = 0.23$, $\omega_i = 0.042$; finally at $X = 2.4$ we have $c = 0.65$, $\omega_r = 0.35$, $\omega_i = 0.035$. Isolines of $|u|$ at $X = 2.2$ are in good agreement with the u_{rms} measured by SB and also present a clear similarity with the u_{rms} computed by Liu and Domaradzki (1993) (see their Fig. 15). However they differ somewhat from the $|u|$ of Yu and Liu (later analyzed in detail by the same authors), e.g. in the present case we find the maximum in the outer part of the boundary layer, while Yu and Liu found the maximum closer to the wall and more concentrated near the outflow region. These differences may be explained by small differences in the basic flow field: The nonlinear calculation by Sabry and Liu was started at $x = 60$ cm, corresponding to $X = 1.5$ in the

present calculations. They computed the flow with a temporal approach and converted to spatial by the adoption of a convection velocity. The general conclusion, however, is the same: The calculations confirm the correlation between u_{rms} and $\partial U/\partial z$, first observed by SB. A complete comparison between our results and those of other investigators for $\Lambda = 450$ is presented in Table II.

A few other modes in the spectrum at $X = 2.4$ are displayed in Figure 14. At high frequencies, the second sinuous mode is concentrated near the outflow at the wall. The distribution of $|u|$ as well as the phase velocity ($c = 0.59$) are almost identical to the high frequency mode found for $\Lambda = 160$ at the same station. Also the two varicose modes are quite similar to the case $\Lambda = 160$: Both of them are centred in the turn-over region in the outer part of the boundary layer. This is particularly true for the fast moving high frequency mode ($c = 0.74$), for which u almost vanishes on the symmetry upwash line (Figure 14c).

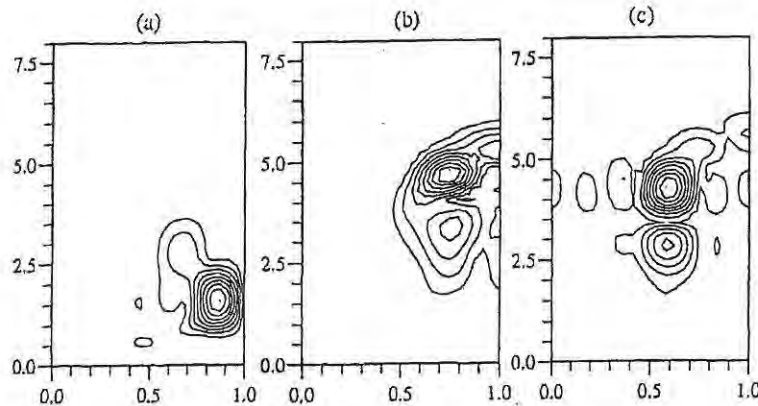


Fig. 14. - $\Lambda = 450$: Isolines of $|u|$ for higher modes at $X = 2.4$: (a) 2nd sinuous mode: $c = 0.59$, $\omega_r = 0.60$, $\omega_i = 0.047$; (b) 1st varicose mode: $c = 0.59$, $\omega_r = 0.37$, $\omega_i = 0.034$; (c) 2nd varicose mode: $c = 0.74$, $\omega_r = 0.68$, $\omega_i = 0.035$.

3.4. DEVELOPMENT FOR $\Lambda = 1000$

Although the physical wave-lengths of the two cases studied above differ by a factor of two, the development of both the primary and the secondary instability is very similar. In this section, we will discuss the development for a yet larger wave-length, which will bring out some important differences. We have chosen $\Lambda = 1000$, which gives a spanwise wave length of 3.065 cm, which is 3.4 times larger than for $\Lambda = 160$ and 1.7 times larger than for $\Lambda = 450$.

Since Görtler vortices grow less rapidly at $\Lambda = 1000$, the stage of development reached at $X = 2.6$ for $\Lambda = 1000$ corresponds qualitatively to the stage reached at $X = 2.2$ when $\Lambda = 160$. This can be seen by comparing the basic flow fields for $\Lambda = 1000$ (Figure 15ab) with those for the lower wave numbers (Figures 3ab and 13ab). Note that the z -axis is normalized with the wave-length and does not show the physical proportions between y and z . At larger Λ , the mushroom structures are further apart, and seem to become more concentrated at the outflow region and less constrained by neighboring vortices. Also, the

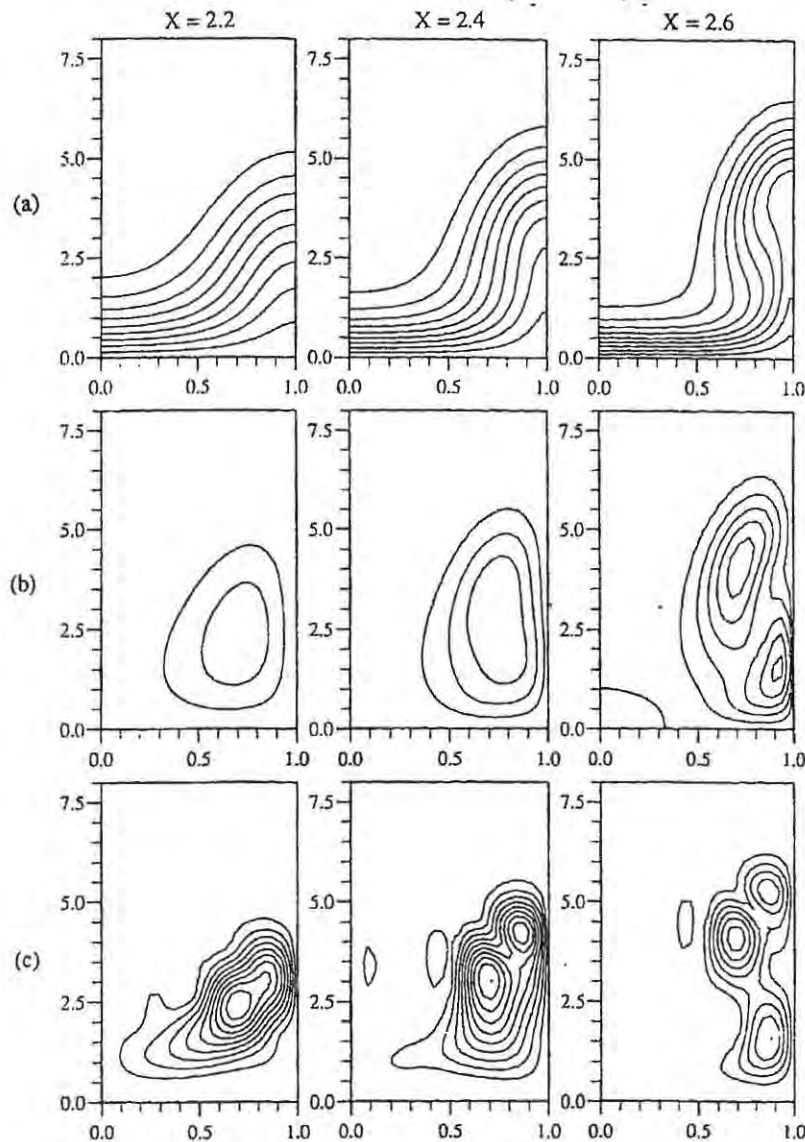


Fig. 15. - $\Lambda = 1000$: Downstream development of U (a), $|\partial U/\partial z|$ (b) and $|u|$ (c) of the most unstable sinuous modes at three values of X . Figures not to scale.

vortices extend further away from the wall for $\Lambda = 1000$ than in the smaller wave-length cases. These features are also reflected in the spanwise decomposition of the flow field (shown in Figure 16). The first harmonic \tilde{U}_1 (representing the spanwise *rms*-distribution of U) is larger than for $\Lambda = 160$ (see Figure 5). It has its maximum near the boundary layer edge, and lacks the second near wall maximum which is present for $\Lambda = 160$. The amplitudes of the higher harmonics increase more rapidly than for $\Lambda = 160$, which means that $N > 5$ is required to adequately represent the vortices past $X = 2.6$.

The eigenvalue maps in Figure 17 show that the sinuous mode dominates at $X = 2.2$ and 2.4. As in the previous cases, we can observe the tendency for ω_r , ω_i and c to increase with X . At $X = 2.6$ the sinuous and varicose modes amplify at about the same rate, but the varicose mode operates on a much wider frequency range. The sinuous

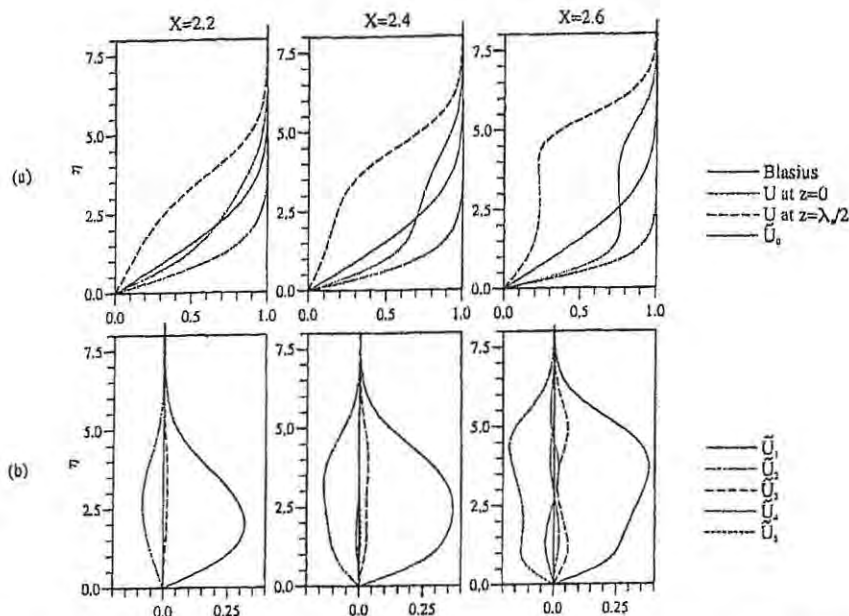


Fig. 16. - $\Lambda = 1000$: Spanwise structure of the Görtler vortices at three values of X . (a) $\tilde{U}_0(\eta; X)$ and $U(\eta; z)$ at $z = 0$ and $\lambda_z/2$, $2D$ Blasius boundary layer profile. (b) spanwise harmonics of $U(\eta)$.

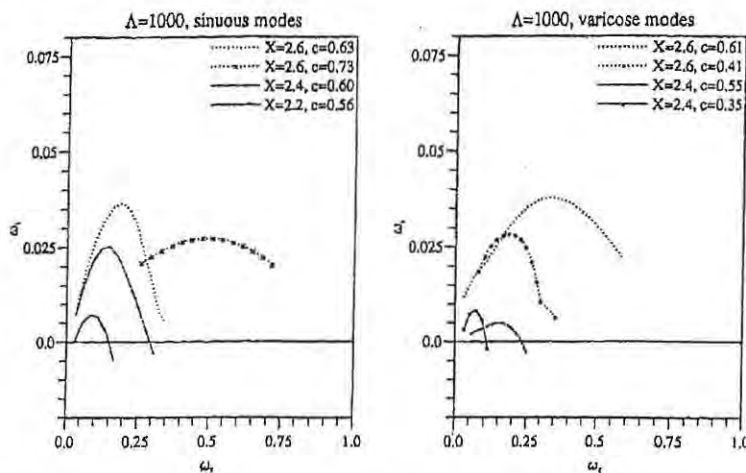


Fig. 17. - $\Lambda = 1000$: Downstream development of the temporal growth rates for the secondary instability.

distributions of $|u|$ corresponding to points of maximum values in Figure 17 are shown in Figure 15c. For this mode we again notice how the downstream evolution of the mode shape coincide with the $\partial U/\partial z$ field, e.g. the development of a near wall maximum at the side of the mushroom stem for $X = 2.6$. A double peak structure appears by the mushroom hat, and this is similar to what was observed by Park (1990), Liu and Domaradzki (1993) and Hall and Horseman (1991); Hall and Horseman, however, did not find any activity close to the wall on either side of the outflow region because wall structures can not be properly accounted for by their inviscid analysis. The shear layers near the mushroom stem are, however, essential for the development of the instability, even when Λ is very large and such shear layers are relatively weak. At $X = 2.4$ and 2.6 we found that other modes can also be triggered: One more sinuous mode (Figure 18a),

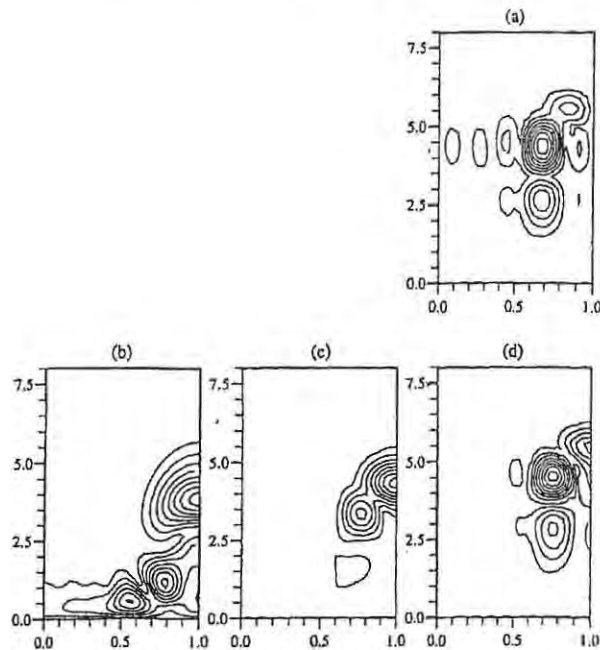


Fig. 18. - $\Lambda = 1000$: Downstream development of $|u|$ for higher modes. (a) $X = 2.6$, second sinuous mode: $c = 0.73$, $\omega_r = 0.48$, $\omega_i = 0.027$; (b) $X = 2.4$, first varicose mode: $c = 0.35$, $\omega_r = 0.07$, $\omega_i = 0.008$; (c) $X = 2.4$, second varicose mode: $c = 0.55$, $\omega_r = 0.15$, $\omega_i = 0.005$; (d) $X = 2.6$, first varicose mode: $c = 0.61$, $\omega_r = 0.35$, $\omega_i = 0.038$.

important in a relatively high frequency range, and three varicose modes (Figure 18bcd). One of the latter (Figure 18b), at $X = 2.4$ and amplified in a low frequency range, is a viscous mode with most of the activity concentrated near the wall. The most salient feature in the development of the varicose modes between $X = 2.4$ and 2.6 is the intensification in the "turn-over" region ($y/\delta = 5$, $2z/\lambda_z = 0.6$).

4. Discussion of the results

A criterion for predicting the onset of the instability in space emerges from the results obtained. When the spanwise-averaged distribution of U develops an inflection point, a sinuous mode with positive growth rate appears. This X location can also be predicted quite accurately by inspection of the shear stress distribution at the outflow plane of the vortices: A secondary instability occurs a little before the location where this stress component is minimum; *cf.* Figure 2, where the crosses denote the locations where the growth rate of the secondary, sinuous instability exceeds zero. It is here that a strongly nonlinear reorganization of the vortices takes place, and well defined "mushrooms" appear; these "mushrooms" carry with them internal shear layers which are responsible for the initiation of the wavy instability (Bottaro *et al.*, 1996). This is the phase where E departs from an exponential growth and approaches saturation. The saturation state might, in fact, never be reached, since the growth rates of the instability are so large that the flow will rapidly become unsteady and undergo transition.

When the spanwise wave length of the vortices is sufficiently small, the perturbations in the streamwise velocity are extremely well correlated with the spanwise rate of strain $\partial U/\partial z$. As λ_z increases, an influence of $\partial U/\partial y$ on the sinuous mode is evidenced through the formation of a double-peaked structure in the isolines of $|u|$, around the flow turn-over region; the increased importance of a varicose instability wave at sufficient downstream distances is also ascribed to the influence of the normal shear.

4.1. RELATION BETWEEN THE SINOUS MODE AND $\partial U/\partial z$

The close correspondance between the u -sinuous mode shape and the spanwise shear $\partial U/\partial z$ of the base flow suggests a scaling on the frequency (or the wave-length, related to the frequency via the phase velocity) of the secondary instability. Roughly we suggest that each mode of the sinuous instability is related to one (or more) areas of intense normal vorticity (equal, to leading order, to the spanwise shear) in the cross-section. For $\Lambda = 160$ and 450 we have established that the first mode that develops in X presents two regions of intense u perturbations, closely matched by extrema in $\partial U/\partial z$ of the base flow. This first mode has a relatively low frequency (at the point of maximum amplification) and, for both wave lengths under consideration, the following relations are found to apply, *independently of X* :

$$(4.1) \quad |\partial U/\partial z|_{\max}/\omega_r = 1.20 \pm 0.05,$$

$$(4.2) \quad |\partial U/\partial z|_{\max}/\alpha = 0.79 \pm 0.05,$$

where $|\partial U/\partial z|_{\max}$ is the maximum value of $\partial U/\partial z$ in the (y, z) plane. These relations are valid at all X -stations for which the growth rate of the most unstable secondary instability sinuous mode far exceeds that of the primary instability: This is also the condition of applicability of a local analysis, which exploits the fact that the base flow field evolves slowly in X . The exception to the rule expressed by relations (4.1) and (4.2) is the station $X = 2$, for $X = 2$, for $\Lambda = 450$ (see Figure 11), for which the rate of amplification of the secondary instability is still quite weak; in this particular case $|\partial U/\partial z|_{\max}/\omega_r = 1.68$ and $|\partial U/\partial z|_{\max}/\alpha = 1.01$. For moderate spanwise wavelengths, we have thus obtained the interesting results expressed by (4.1) and (4.2).

For $\Lambda = 1000$ the development of both primary and secondary instabilities is slower and the outlook is not as promising: The upwash of the vortices is more pronounced and extends far outside the nominal Blasius boundary layer, and the downturn of the flow (the formation of the mushroom) is not as pronounced as for the smaller spanwise wave-length cases; also, and more importantly, the maximum values of the normal shear $\partial U/\partial y$ at the mushroom's hat become larger than the maxima in spanwise shear, at all X 's. These characteristics of the flow already indicate a preference towards a different mode of instability, a mode which chooses a different symmetry and favours perturbations in v , rather than w . This is confirmed by our stability calculations: The sinuous mode appears first, but grows more slowly than the varicose mode (see Figure 17); the latter becomes predominant for $X \geq 2.6$ because of the influence of the normal shear (see also

Saric, 1994). The close correspondence that existed for smaller values of Λ (particularly for $\Lambda = 160$) between the u -fluctuations of the sinuous mode and $\partial U/\partial z$ is not present any more and the isolines of $|u|$ show a well defined "extra" region of oscillations on either sides of the upwash line, by the mushroom's hat (Figure 15c). Clearly, in this case we can not focus only on the spanwise shear but must look at the combined influence of spanwise and normal shear; examination of the maximum value of $\partial U/\partial y$ close to the hat for $2z/\lambda_z = 1$ reveals that $|\partial U/\partial y|_{\max}$ is typically twice as large as $|\partial U/\partial z|_{\max}$, at all X 's. For $\Lambda = 160$ exactly the opposite occurred, whereas at 450 the values of maximum normal and spanwise shears were comparable. The combination of normal and spanwise shear rules the instability development, but, somewhat surprisingly, the scaling proposed in (4.2) for the streamwise wave number α still holds; the frequency selected by the instability is slightly different from before and it is now found to vary, for all unstable X 's examined, according to the relation

$$(4.3) \quad |\partial U/\partial z|_{\max}/\omega_r = 1.41 \pm 0.08.$$

Our simple linear relations between frequency and maximum spanwise shear are reminiscent of that proposed by Monkewitz and Huerre (1962) for the case of the mixing layer. They have shown that, almost independently of the velocity ratio, the frequency of the spatial travelling wave instability of a symmetric mixing layer scales as:

$$(4.4) \quad \frac{|\partial U/\partial z|_{\max}}{\omega_r} = 1.22 \frac{(U_{\max} - U_{\min})}{(U_{\max} + U_{\min})/2},$$

where U_{\max} and U_{\min} are the upper and lower velocities in the mixing layer. It would be worthwhile to try to derive a similar "universal" expression for the symmetric wake distribution and compare with (4.1) and (4.3): A favourable comparison would support the argument by Sabry *et al.* (1990) and Le Cunff and Bottaro (1993) that the secondary sinuous instability of longitudinal vortices is driven by (and can be explained through) the local instability of the wake profile that is established at the normal position of largest spanwise shear, and that mechanisms in the direction normal to the wall represent higher order effects.

A possibly important second sinuous mode in the large frequency range has been discovered for all wavelengths. This mode acquires importance as X increases, and for $\Lambda = 160$ and 450 it contains exclusively u -oscillations localized at the side of the mushroom stem (e.g. $(2z/\lambda_z, y/\delta) = (0.9, 1.3)$ for $X = 2.4$, $\Lambda = 450$), as shown on Figures 10a and 14a. For the large wavelength case ($\Lambda = 1000$) the second sinuous mode is concentrated in the turn-over region $(2z/\lambda_z, y/\delta) = (0.66, 4.5)$ as shown in Figure 18a, and presents higher phase velocity when compared to the other second sinuous modes of smaller Λ . There do not appear to be simple scaling relationships for this mode.

4.2. EFFECTS OF REYNOLDS NUMBER AND CROSS-STREAM VELOCITY COMPONENTS

In all cases studied above, the sinuous mode becomes unstable first. The importance of the varicose mode increases with X , however, but for $\Lambda = 160$ and 450 its growth

rate never exceeds that of the sinuous mode. This appears to be in contrast with some experimental evidence which shows a predominance of horseshoe shaped secondary instabilities (Bippes 1978, Aihara 1993), *i.e.* instabilities which are symmetric with respect to the primary vortex. Clearly, the experimental visualizations represent finite amplitude effects, beyond the range of a linear approach; furthermore, it is the spanwise wavenumber which determines the least stable symmetry, and varicose modes do dominate far enough downstream for $\Lambda = 1000$. Still, we set out to examine some further aspects which may play a role in the mode selection. In Figure 19 we have plotted the most unstable modes for $\Lambda = 160$ ($X = 2.2$) and for $\Lambda = 1000$ ($X = 2.6$), for a few values of the Reynolds number, Re . The only effect of Re is visible for the smaller spanwise wave

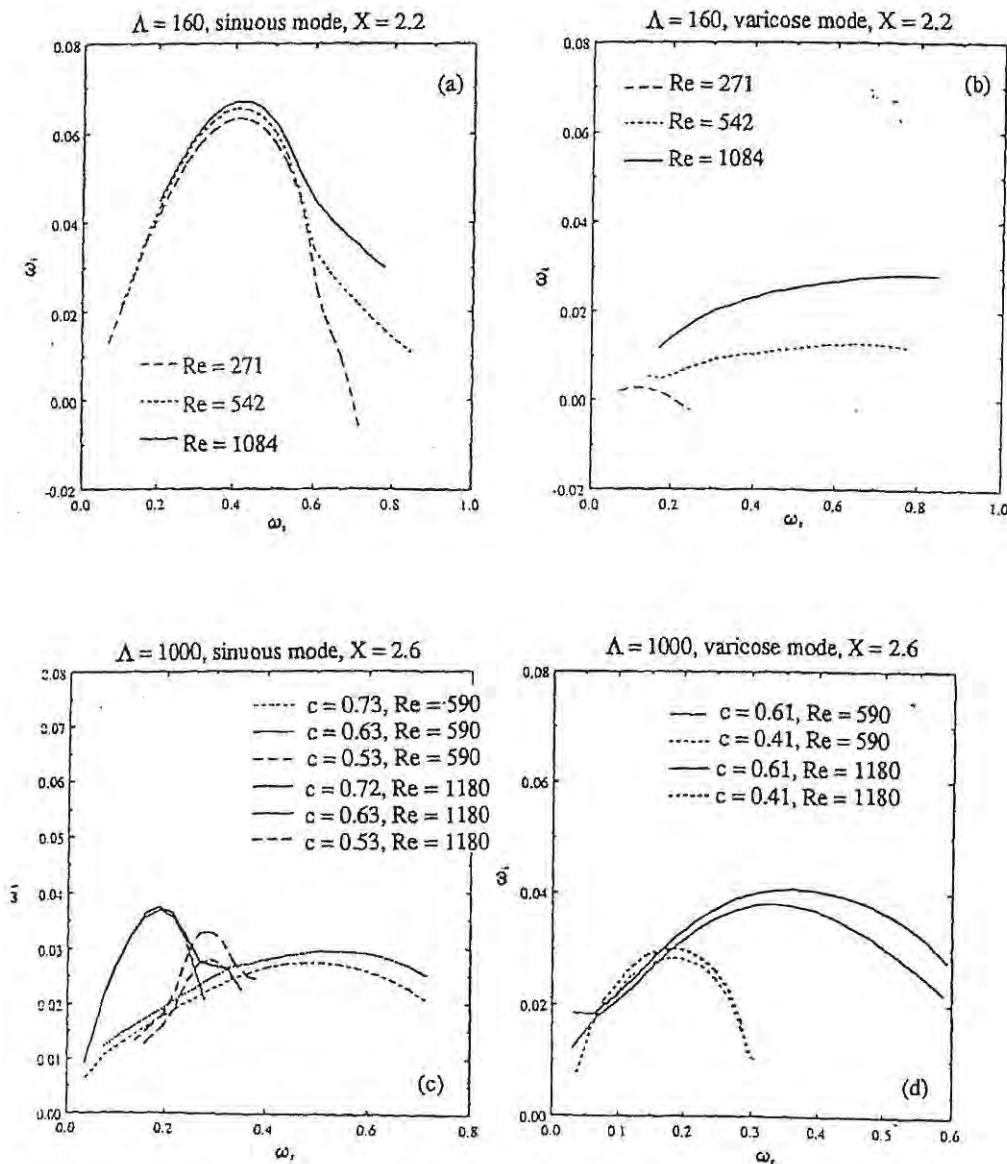


Fig. 19. – Effect of varying the Reynolds number.

length (Figure 19ab): increasing the Reynolds number results in a destabilization of the varicose mode: ω_i increases and so does the range of unstable ω_r 's. This mode does not, however, succeed in overcoming the sinuous mode at the streamwise positions examined. When Λ is large (Figure 19cd) the effect of Re is insignificant; this is indicative of the fact that the importance of the varicose mode here has to be entirely attributed to the structure of U . In Figure 20 we compare, for the sinuous mode at $\Lambda = 160$, the effect of increasing Re to that of including the cross-stream velocity components in the analysis. These effects are comparable: They both result in a slight (almost negligible) destabilization of the mode.

We have thus found a relatively small influence of nonparallel terms on the different modes of the instability. The more significant deviations occur on the varicose mode for small Λ , but the sinuous mode remains dominant throughout.

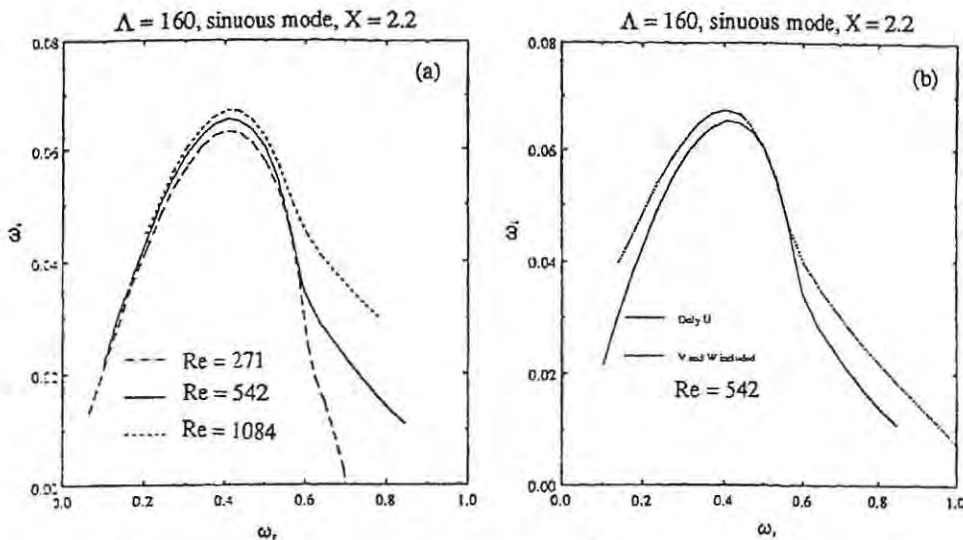


Fig. 20. – Comparison between the effect of varying the Reynolds number (a) and that of including in the analysis the cross-flow velocity components V and W (b).

5. Summary and conclusions

A linear stability analysis of the secondary instability of the Görtler flow has been carried out, and for the first time predictions of frequency and wave length, based on a criterion of maximum linear amplification, have been presented, for a number of downstream flow stations, and for a wide range of spanwise wave lengths.

We have established that the neglect of nonparallel terms (as in Hall and Horseman 1991; Yu and Liu 1991, 1994) is justified in the analysis of the sinuous mode, whereas a small Re influence appears for small Λ on the varicose mode of instability. At early streamwise locations where the instability becomes operational, however, the sinuous mode always remains dominant.

The results obtained support the conclusion that one crucial factor in the breakdown of Görtler vortices is the spanwise wave length of the primary vortex flow. Furthermore, it is established that:

(i) The sinuous mode of instability is always destabilized first, and the onset of the instability coincides with the development of an inflection point in the spanwise-averaged distribution of U ;

(ii) The u -fluctuating field of the sinuous mode is well correlated with $\partial U/\partial z$ at low Λ , whereas for large values of Λ an influence of the normal shear on $|u|$ is present. The influence of the normal shear at large Λ is also felt in the increased importance of the varicose mode of instability;

(iii) The most unstable frequency of the sinuous instability grows with $|\partial U/\partial z|_{\max}$ (and with X) and for the case of air flow can be expressed quite precisely by:

$$F \approx 0.13 \left| \frac{\partial U}{\partial z} \right|_{\max},$$

whereas the streamwise wave-length λ_x is related to the shear through:

$$\lambda_x \left| \frac{\partial U}{\partial z} \right|_{\max} \approx 5 U_{\infty}.$$

These are valid almost independently of the spanwise wave-length and streamwise distance, and apply remarkably well to the results of SB at $x = 100$ cm (for which $|\partial U/\partial z|_{\max} \approx 1000$ Hz, $\lambda_x = 2.5$ cm and $F = 130$ Hz). This result indicates that the three-dimensional aspect of an inflectional instability such as the present one can be qualitatively interpreted on the basis of very simple local arguments.

(iv) With the increase of the streamwise distance the varicose instability becomes important, and this is consistent with the downstream observation of horseshoe shaped vortices in several experiments (Bippes 1978, SB, Aihara 1993) and simulations (Liu and Domaradzki 1994).

Our study corroborates and completes previous experimental and theoretical works on the secondary instability of Görtler vortices (SB, Park 1990, Park and Huerre 1995, Hall and Horseman 1991, Yu and Liu 1991, 1994). Some aspects of the present results can also be extrapolated to more complex flow situations, and Park (1990) has already shown how a sinuous instability of vortices can be interpreted as a process similar to a lift-up of low speed streaks in a turbulent boundary layer. Much work remains to be done, however, and in particular the nonlinear development of the instability, already approached by Liu and Domaradzki (1994), awaits further investigation. One interesting development concerns the nonlinear interaction between sinuous and varicose waves, and the subsequent fast breakdown of vortices, when the base flow is weakly asymmetric about the upwash plane (Wallace *et al.*, 1994).

Acknowledgements

This paper is dedicated to the memory of Prof. Inge L. Ryhming, a mentor and friend.

The project was supported by the Swiss National Fund under grant no. 21-36035.92 and by the Swedish Technical and Scientific Research Council. The steady Görtler flows used as a basis for the secondary stability analysis were obtained together with Prof. A. Zebib; he and Prof. P. A. Monkewitz are acknowledged for interesting discussions and for reading and commenting upon the original manuscript. One referee is acknowledged for a very thorough review. Computational resources were generously supplied by the computing centre of EPFL.

REFERENCES

- AIHARA Y., 1993, Personal communication.
- BASSOM A. P., SEDDOUGUI S. O., 1990, The onset of time-dependence and three-dimensionality in Görtler vortices: neutrally stable wavy modes, *J. Fluid Mech.*, **220**, 664.
- BIPPES H., 1978, Experimental study of the laminar-turbulent transition on a concave wall in a parallel flow, *NASA TM*, 75243.
- BOTTARO A., KLINGMANN B. G. B., ZEBIB A., 1996, Görtler vortices with system rotation, In press, *Theo. Comp. Fluid Dyn.*
- DEAN W. R., 1928, Fluid motion in a curved channel, *Proc. Roy. Soc. London*, **A121**, 402.
- FLORYAN J. M., SARIC W. S., 1984, Wavelength selection and the growth of Görtler vortices, *AIAA J.*, **22**, 1529.
- GUO Y., FINLAY W. H., 1994, Wavenumber selection and irregularity of spatially developing nonlinear Dean and Görtler vortices, *J. Fluid Mech.*, **264**, 1.
- HALL P., HORSEMAN N. J., 1991, The linear inviscid secondary instability of longitudinal vortex structures in boundary layers, *J. Fluid Mech.*, **232**, 357.
- HALL P., SEDDOUGUI S. O., 1989, On the onset of three-dimensionality and time-dependence in Görtler vortices, *J. Fluid Mech.*, **204**, 405.
- KLINGMANN B. G. B., 1993, Linear parabolic stability equations applied to three-dimensional perturbations in a boundary layer, *Rep*, T-93-12, IMHEF-DME, Swiss Federal Institute of Technology, Lausanne.
- LE CUNFF C., BOTTARO A., 1993, Linear stability of shear profiles and relation to the secondary instability of the Dean flow, *Phys. Fluids, A*, **5**, 2161.
- LEE K., LIU J. T. C., 1992, On the growth of mushroomlike structures in nonlinear spatially developing Görtler vortex flow, *Phys. Fluids, A*, **4**, 95.
- LIU W., DOMARADZKI J. A., 1993, Direct numerical simulation of transition to turbulence in Görtler flow, *J. Fluid Mech.*, **246**, 267.
- MONKEWITZ P. A., HUERRE P., 1982, Influence of the velocity ratio on the spatial instability of mixing layers, *Phys. Fluids*, **25**, 1137.
- PARK D. S., 1990, The primary and secondary instabilities of Görtler flow, *Ph. D. Thesis*, Univ. of Southern California.
- PARK D. S., HUERRE P., 1995, Primary and secondary instabilities of the asymptotic suction boundary layer on a curved plate, *J. Fluid Mech.*, **283**, 249.
- PATANKAR S. V., SPALDING D. B., 1972, A calculation procedure for heat, mass and momentum transfer in three-dimensional parabolic flows, *Int. J. Heat Mass Transfer*, **15**, 1787.
- PEXIEDER A., TRUONG T. V., MAXWORTHY T., MATSSON J. O. E., ALFREDSSON P. H., 1993, Görtler vortices with system rotation: experimental results, In *Spatio-Temporal Properties of Centrifugal Instabilities*, NATO Advanced Research Workshop, Nice, France, March 28-29.
- SABRY A. S., YU X., LIU J. T. C., 1990, Secondary instabilities of three-dimensional inflectional velocity profiles resulting from longitudinal vorticity elements in boundary layers, In *IUTAM Symposium on Laminar-Turbulent Transition*, Toulouse, France, September 11-15, 1989. D. Arnal and R. Michel eds., Springer Verlag, Berlin, 441.
- SABRY A. S., LIU J. T. C., 1991, Longitudinal vorticity elements in boundary layers: nonlinear development from initial Görtler vortices as a prototype problem, *J. Fluid Mech.*, **231**, 615.

- SARIC W. S., 1994, Görtler vortices, *Annu. Rev. Fluid Mech.*, **26**, 379.
- SEDDOUGUI S. O., BASSOM A. P., 1991, On the instability of Görtler vortices to nonlinear travelling waves, *IMA J. Applied Math.*, **46**, 269.
- SWEARINGEN J. D., BLACKWELDER R. F., 1987, The growth and breakdown of streamwise vortices in the presence of a wall, *J. Fluid Mech.*, **182**, 255.
- WALLACE D., REDEKOPP L. G., HUERRE P., 1994, Resonantly interacting modes in wake shear layers, *Eur. J. Mech. B/Fluids*, **13**, 139.
- WOLFRAM S., 1991, *Mathematica*, Addison-Wesley Publishing Co., Redwood City, California.
- YU X., LIU J. T. C., 1991, The secondary instability in Goertler flow, *Phys. Fluids, A*, **3**, 1845.
- YU X., LIU J. T. C., 1994, On the mechanism of sinuous and varicose modes in three-dimensional viscous secondary instability of nonlinear Görtler rolls, *Phys. Fluids*, **6**, 736.

(Manuscript received November 18, 1994;
revised November 17, 1995; accepted December 12, 1995.)